A Three-Dimensional Planetary Boundary Layer Model for the Somali Jet

T. N. KRISHNAMURTI, VINCE WONG,[1] HUA-LU PAN,[2] RICHARD PASCH, JOHN MOLINARI[3] AND PHILIP ARDANUY[4]

Department of Meteorology, Florida State University, Tallahassee 32306

(Manuscript received 22 March 1982, in final form 20 December 1982)

ABSTRACT

This paper is an extension of an earlier study on the planetary boundary layer dynamics of the low level monsoonal flow over the Arabian Sea (Krishnamurti and Wong, 1979), where the long term steady state motion field for a boundary layer was determined using a zonally symmetric model with a prescribed pressure field. In that study we examined the balance of forces in the surface layer and the planetary boundary layer for regions across the equator, across and along the low-level Somali jet, and across an intertropical convergence zone. The important role of advective accelerations in the near-equatorial balance of forces was demonstrated. The present study is based on a three-dimensonal model that removes the restriction of zonal symmetry. This mesoscale fine mesh model, with a horizontal resolution of ~55 km and a vertical resolution of 200 m, is integrated to examine the evolution of three-dimensional planetary boundary layer flows for prescribed three-dimensional pressure patterns. The observations of the pressure field were obtained from the climatological analysis of Van De Boogaard (1977) and the MONSOON 77 and MONEX 1979 data sets. The results of these long term integrations and the balance of forces are discussed and compared with those inferred from cross-equatorial trajectories of constant level balloons.

1. Introduction

A classification of the large scale planetary boundary layer into Ekman, advective and Stokes (time dependent) force balances was presented by Mahrt and Young (1972). Fig. 1 identifies this separation based on a scaling argument of the equations of motion (lists of symbols and acronyms appear in the appendix.

$$\frac{\partial u}{\partial t} + u\frac{\partial u}{\partial x} + v\frac{\partial u}{\partial y} + w\frac{\partial u}{\partial z} - fv = -\frac{1}{\rho}\frac{\partial p}{\partial x} + F_x. \quad (1)$$

On a beta-plane we may use the following scaling relations,

$$(u, v, w) = U\cdot(u', v', w'), \quad (2)$$

$$\frac{\partial}{\partial(x, y, z)} = \left(\frac{\beta}{U}\right)^{1/2}\frac{\partial}{\partial(x', y', z')}, \quad (3)$$

$$f = \beta y, \quad (4)$$

$$\frac{\partial}{\partial t} = \omega\frac{\partial}{\partial t'}, \quad (5)$$

and obtain

$$\omega\left(\frac{\partial u'}{\partial t'}\right) + (U\beta)^{1/2}\left[u'\frac{\partial u'}{\partial x'} + v'\frac{\partial u'}{\partial y'} + w'\frac{\partial u'}{\partial z'}\right] - \beta y v' = \frac{P}{U} + \frac{F}{U}. \quad (6)$$

Here ω is a characteristic frequency, U a velocity scale, and P and F denote the pressure gradient and frictional forces. In this context three possible time scales may be identified as ω^{-1}, $(U\beta)^{-1/2}$, and $(\beta y)^{-1}$. A distinction of the boundary layer dynamics may be obtained for the following three cases:

1) $\omega < \beta y, \quad (U\beta)^{1/2} < \beta y.$

In this case the balance would be between the Coriolis, pressure gradient, and frictional forces, *i.e.*, so-called Ekman balance.

2) $\omega < (U\beta)^{1/2}, \quad \beta y < (U\beta)^{1/2}.$

In this case the balance is among the advective, pressure gradient and frictional forces, and is usually designated as the advective boundary layer.

3) $\omega > \beta y, \quad \omega > (U\beta)^{1/2}.$

In this case the time dependent high frequency local accelerations have a balance with respect to the pressure gradient and frictional forces and we have what is called a Stokes balance. Fig. 1 separates these balances according to the above relations on the ω–f plane.

Current affiliations:
[1] Systems and Applied Sciences Corporation, Hampton, Virginia 23666.
[2] Oregon State University, Corvallis, Oregon, 97331.
[3] State University of New York, Albany, New York, 12222.
[4] Research and Data Systems, Lanham, Maryland 20801.

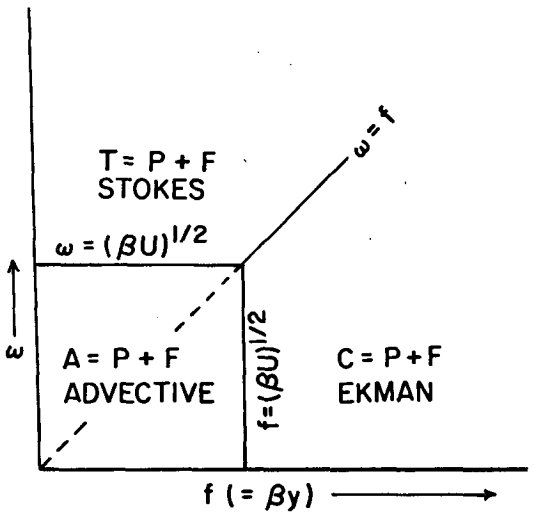

FIG. 1. Regimes in the boundary layer (after Mahrt and Young, 1972).

In this paper we examine the large scale dynamics of the planetary boundary layer over the Arabian Sea. Our interest lies in the transition of the boundary layer across the equator, across and along the low level jet and across the intertropical convergence zone during northern summer. This is a three-dimensional study, and is an extension of an earlier work in two dimensions (Krishnamurti and Wong, 1979). In the two-dimensional model, an equilibrium motion field with respect to a pressure field prescribed from observations was obtained from a long term (~50 days) integration of a high resolution boundary layer model on a meridional-vertical plane at 60°E. The prescribed pressure field varied with height so that baroclinic effects in the boundary layer were retained. The principal results are summarized in Fig. 2. Near the ocean surface, in a surface layer, the essential balance is between the pressure gradient and frictional forces. In the overlying friction layer, as one proceeds northward from 15°S, Ekman balance is dominant until one reaches ~10°S. The equatorial region is characterized by a balance between the pressure gradient, horizontal advective, and frictional forces. Poleward in both directions from this equatorial region, Coriolis force becomes significant. As a result, winds back with height to the south, and veer with height to the north, producing diffluence and a region of descending motion in the equatorial friction layer.

The low-level jet, in the two-dimensional simulation, lies at ~11°N. A slow veering of westerly winds occurs south of this latitude, and a more rapid veering occurs to the north. This configuration results in a convergence of both mass and momentum flux at the latitude of the jet. The region of the ITCZ near 12°N is dominated by strong vertical advection associated with ascending motion above a region of large Ekman convergence on the cyclonic shear side of the strong low-level jet. Furthermore, the region is surrounded by an Ekman balance north of 15°N, and by a horizontally advective boundary layer south of 10°N.

The two-dimensional analysis precluded the possibility of a Stokes regime in the boundary layer due to specification of a time-independent pressure field. In the present study, pressure is also specified from observations, but in three-dimensions. To minimize the potential limitations arising from this fixed pressure field, initial states were chosen from available data sets during periods when the flow and pressure patterns showed the least variation from day to day. Although it is impossible to have an exact steady state at every point in nature, this procedure insures that significant flow changes are not occurring at the time the pressure field is chosen. As in the two-dimensional study, the model equations are started from a state of Ekman balance (except near the equator), and integrated to an eventual steady state.

Reverdin and Sommeria (1981), have examined the balance of forces along the low level balloon tra-

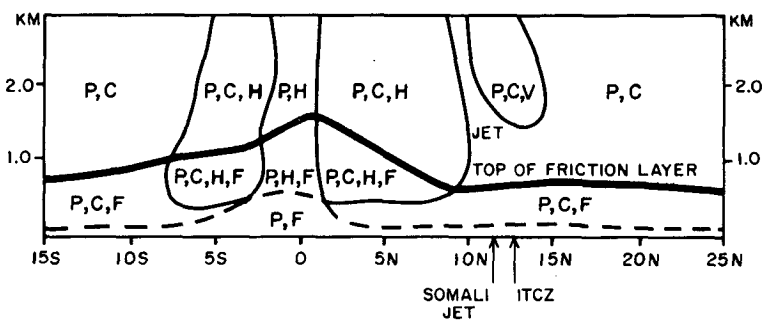

FIG. 2. A schematic illustration of various regimes and significant forces in the boundary layer, from day 50 of the two-dimensional simulation of Krishnamurti and Wong (1979). The letters *P*, *C*, *H*, *V* and *F* stand, respectively, for pressure gradient, Coriolis, horizontal and vertical advective, and frictional forces. Only those relative forces with a magnitude exceeding 0.3 are identified for each regime. The dashed line represents the top of the surface layer, and the solid line the top of the friction layer.

jectories (the BALSAMINE Experiment) at the 1-km level over the Arabian Sea. Their studies include an analysis of the pre-onset period, 15–30 May 1979. During this period they estimated the various terms of the horizontal equation of motion from the balloon data and, for the pressure gradient force, from the daily final FGGE IIIb analysis. Their results, for a typical case shown in Fig. 3, illustrate the transitions in the balance of forces for a cross-equatorial trajectory. Because Reverdin and Sommeria's equation was written with the residual friction force on one side, and the Coriolis force and pressure gradient force with the acceleration term on the other side, the arrows for $f\mathbf{k} \times \mathbf{V}_H$ and $\nabla_p\phi$ point opposite to the usual convention. The vector sum of the three terms equals **F**. In this diagram, $\mathbf{V}_b$ denotes the vector motion along the balloon trajectory, and $\mathbf{V}_G$ denotes the surface wind vector from the ECMWF analysis. The balance of forces (per unit mass) is shown for three near-equatorial points along the trajectory, two in the Southern Hemisphere and one in the Northern Hemisphere. For the two Southern Hemisphere points, it is seen that the horizontal acceleration vector is to the right of and slightly opposite to the flow, consistent with the deceleration and clockwise curving along the trajectory south of the equator. Just north of the equator the acceleration is still to the right of the flow, but with a component in the direction of the trajectory, implying an increase of speed and a continued clockwise turning in the Northern Hemisphere. The pressure gradient, fairly constant along the portion of the trajectory shown here, indicates higher pressure over the southwest Indian Ocean. It is directed nearly perpendicular to the motion over the southern part of the trajectory, but has more of a component opposite to the flow in the near equatorial zone. Thus, the component of cross-isobaric motion (towards lower pressure) increases as the equator is approached. The Coriolis acceleration nearly balances the pressure gradient at the southernmost point of the trajectory (near 3.5°S) but is, of course, very small at the two points nearer to the equator. The drag force, computed as a residual, is nearly opposite to the flow and of a magnitude comparable to that of the pressure gradient or horizontal acceleration for the points south of the equator, but it is comparatively much smaller just to the north of the equator. This again emphasizes the fact that just north of the equator the flow is accelerated, with little impediment, towards lower pressure in the case shown here.

Another related study of a single trajectory essentially following the Somali jet, was presented by Young (1981). Here the data source was the cloud winds derived from the motion of low level cloud tracers monitored from the geostationary satellite. This represents winds close to the 1 km level. The winds thus obtained were used to directly infer the advective acceleration, the Coriolis force and the frictional force (frictional force **F** being proportional to $-k\mathbf{V}$), while the pressure gradient force was obtained as a residual. This Gulberg–Mohn type frictional force always points in a direction opposite to the velocity vector. The results of Young (1981), shown in Fig. 4, illustrate an essentially geostrophic balance south of 5°S. Downstream from the equator in the

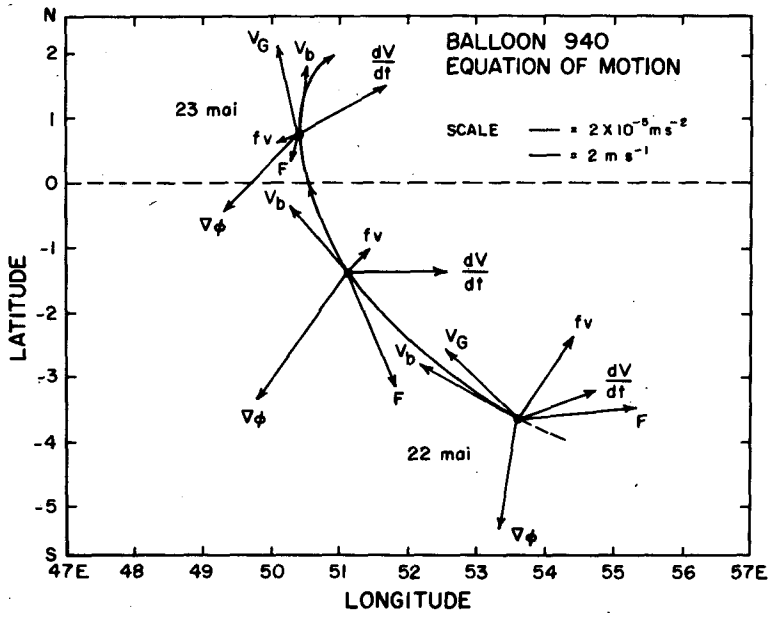

FIG. 3. Balance of forces for selected points along a balloon trajectory at the 1 km level (following Reverdin and Sommeria, 1981). See text for sign conventions and symbols.

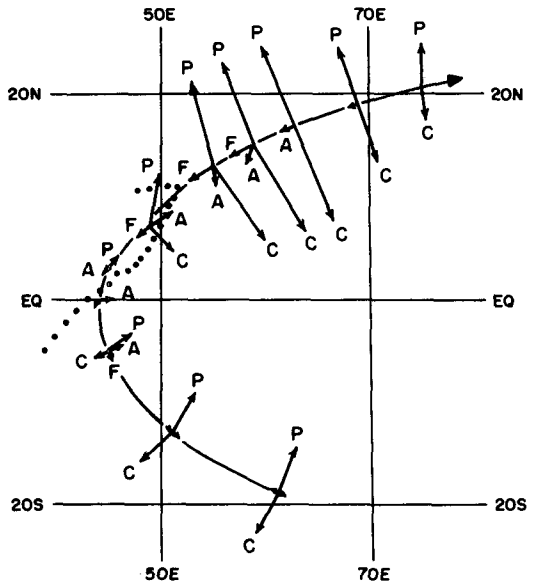

FIG. 4. Balance of forces along a cross-equatorial trajectory, from low-level cloud-motion vectors, following Young (1981). Here *A* is the advective acceleration vector; other symbols as in Fig. 2.

region of the accelerating winds, the advective accelerations point along the direction of the wind, and downstream from the velocity maximum of the Somali jet (12°N and 55°E) the advective accelerations point opposite to the direction of flow. Beyond 17°N, one notes again the geostrophic balance. Young's observational study does not emphasize the role of advective acceleration in regions of strongly curved flows near the equator, a feature that is most conspicuous in the analysis of Reverdin and Sommeria (1981), shown in Fig. 3. The present study uses observations which are taken from MONSOON 77 and MONEX 1979 data, to obtain a balance of forces within the framework of a multi-level, meso-scale boundary layer model.

2. The three-dimensional model

Shallow Boussinesq equations are used in the present study. The equations of motion are:

$$\frac{\partial u}{\partial t} = -u\frac{\partial u}{\partial x} - v\frac{\partial u}{\partial y} - w\frac{\partial u}{\partial z} + fv - \frac{1}{\rho}\frac{\partial p}{\partial x} + F_x, \quad (7)$$

$$\frac{\partial v}{\partial t} = -u\frac{\partial v}{\partial x} - v\frac{\partial v}{\partial y} - w\frac{\partial v}{\partial z} - fu - \frac{1}{\rho}\frac{\partial p}{\partial y} + F_y, \quad (8)$$

and the mass continuity equation is:

$$\frac{\partial u}{\partial x} + \frac{\partial v}{\partial y} + \frac{\partial w}{\partial z} = 0. \quad (9)$$

Density ρ is a function of z only (see Appendix for other symbols). The distribution of pressure, $p(x, y, z)$, is assumed to be known from observations. The horizontal and vertical structure of the model is illustrated in Fig. 5. The model contains a possible maximum of 16 vertical levels and the top boundary is always located at the 3 km level. The treatment of coastal mountains is described below. We use a vertical resolution of 200 m and a horizontal resolution of ~55 km. The lowest layer (a surface layer) is 35 m deep. The level designated by the letter *s* is the top of this surface layer.

Variables are not staggered in the horizontal plane. The computational domain extends from 25°S to 25°N and 25 to 75°E. The three-dimensional array consists of a total of 163 216 grid points over which the variables are defined. The other features of the model are presented below.

We now discuss the dynamics of the near-neutral boundary layer and the frictional forces F_x and F_y. Support for neglecting the effects of stability comes from the observational study of Rubinstein (1981). Using his Figs. 4–5, a bulk Richardson number can be determined in the range of 0.01–0.03, giving a value of Z/L (L the Monin–Obukhov length) of 0.3–0.5, which should allow, as a first approximation, the neglect of stability effects.

The stress at the surface is equated to the stress at the first level Z_+, above the level *s*, by the relation

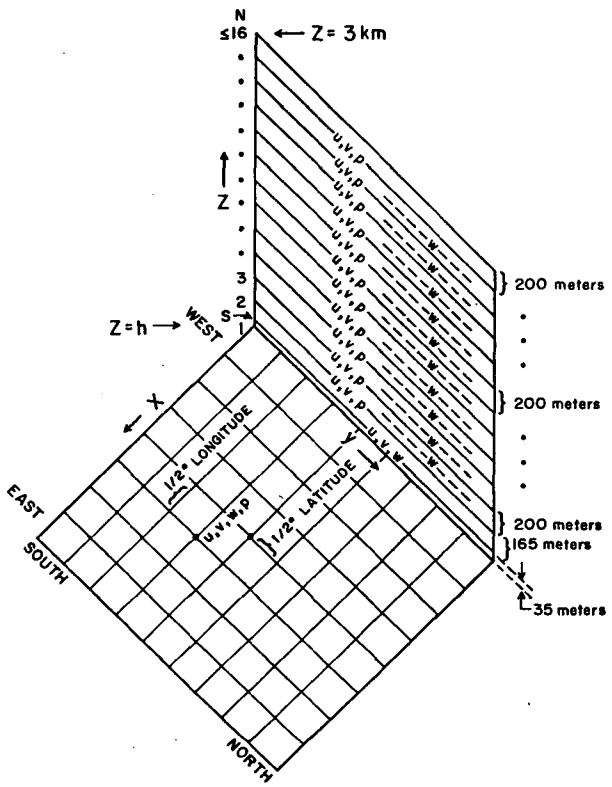

FIG. 5. Geometry of the three-dimensional planetary boundary layer model.

$$C_D|\mathbf{V}_s|\mathbf{V}_s = \left[\frac{k}{\ln\left(\frac{Z_s + Z_0}{Z_0}\right)}\right]^2 |\mathbf{V}_s|\mathbf{V}_s = K\frac{\mathbf{V}_+ - \mathbf{V}_s}{Z_+ - Z_s}, \quad (10)$$

where C_D is the drag coefficient, k the Von Karman constant, and the subscript + denotes the first computational level above the surface layer (see Fig. 5). If the surface roughness Z_0 and the vertical eddy diffusion coefficient K are specified, the surface wind $\mathbf{V}_s$ can be determined *via* the above diagnostic relation. Eq. (10) implies that the direction of the surface wind is the same as that for level +. The surface roughness Z_0 is modeled after Miyake *et al.* (1970) and Fiedler and Panofsky (1972). Table 1 illustrates typical values of Z_0 as a function of topography.

The vertical eddy diffusion coefficient K is designed following Krishnamurti and Wong (1979). Here we define a dissipation length scale λ, by the relation

$$\lambda = \tau^{3/2}/\epsilon \quad (11)$$

where ϵ denotes the energy dissipation and τ represents the magnitude of eddy momentum flux, i.e.,

$$\tau = (\overline{u'w'}^2 + \overline{v'w'}^2)^{1/2}. \quad (12)$$

For a given height of the boundary layer H, Krishnamurti and Wong (1979) have illustrated plots of λ/H *versus* z/H for several different types of near-neutral boundary layer flows and noted that a relation

$$\lambda/H = 0.4\, z/H(1 - 0.92\, z/H)^{1.45}, \quad (13)$$

provides a best fit relation between λ/H and z/H. This functional form was used to parameterize the dissipation ϵ and thus to define a vertical eddy diffusion coefficient K, i.e.,

$$\tau^2/K = \epsilon = \tau^{3/2}/\lambda, \quad (14)$$

hence

$$K = \lambda\tau^{1/2} = \lambda^2|\partial\mathbf{V}_H/\partial z|. \quad (15)$$

The u, v profiles obtained from such a formulation of K for the one-dimensional stationary case have been compared with the higher order closure scheme of Wyngaard and Rao (1974), and a strong similarity was noted in the results for the neutral case. The tests of this scheme in the two-dimensional zonally symmetric boundary layer model of the Somali jet were realistic. The present study is based on this same formulation.

The mountain heights (denoted by $z = h$) were defined from the 1° latitude/longitude tabulations of Gates and Nelson (1975). The values at the ½° grid array in this study were obtained by linear interpolation and are shown in Fig. 6. No further smoothing of the mountain heights was made.

TABLE 1. Roughness length as a function of elevation h.

h (m)	0	200	400	600	800	1000	2000	3000
Z_0 (m)	2.5×10^{-4}	0.24	0.28	0.32	0.36	0.40	1.15	1.15

At levels $z < h$ in the model, $u = v = 0$. A no-slip boundary is present at $z = h$, so that the effects of the mountains appear one grid point away. Lateral convergence (or divergence) gives rise to an upward (downward) motion adjacent to the mountains *via* the continuity equation (9). Fig. 7 shows an example of vertical motion over oceans at the 1 km level which illustrates the effect of coastal mountains. With this simple prescription of mountains it is possible to include rather steep mountains, as is evident in this diagram. The mass field is prescribed and is invariant with respect to time; the flows adjust to an equilibrium state and exhibit both components of the effects of mountains, *i.e.*, flows over and around the mountains.

We shall next address the computational aspects. As in the previous study (Krishnamurti and Wong, 1979) we use the upstream differencing scheme for the nonlinear advective terms. Although this is known to be a damping scheme, this is not a critical problem here since we start from an Ekman solution and build the strong low-level jet. A steady source of energy in this simulation is provided by the internal and potential energy of the prescribed time invariant pressure field. In determining the balance of forces we have used the same finite difference analogs as in the model to avoid incompatible residuals, and the momentum budget is thus exactly balanced.

Centered time differencing is used in this study, except for an occasional use of forward differencing every 50 time steps in order to suppress the splitting of solutions that arises in the well-known leapfrog method. To satisfy the linear stability criterion for diffusion, a time step of 45 s was chosen.

For the evaluation of $u(\partial u/\partial x)$, $v(\partial u/\partial y)$, $u(\partial v/\partial x)$ and $v(\partial v/\partial y)$ at the lateral boundaries, we use upstream boundary conditions at outflow points, and we set advection = 0 at the inflow points. In the evaluation of $w(\partial u/\partial z)$ and $w(\partial v/\partial z)$ at the top boundary:

1) if $w > 0$, upstream boundary conditions are used;

2) if $w < 0$ and the vertical shear of the wind component is positive, vertical advection is set to zero; and

3) if $w < 0$ and the vertical shear is negative, one-sided differences are used.

Condition 2) prevents instability arising from an infinite momentum source when vertical shear is positive and vertical motion downward, a situation that rarely occurred in the simulation. The above boundary conditions were tested and found to provide the most realistic simulation of vertical shear of the horizontal wind.

At the bottom boundary ($z = h$), the vertical ad-

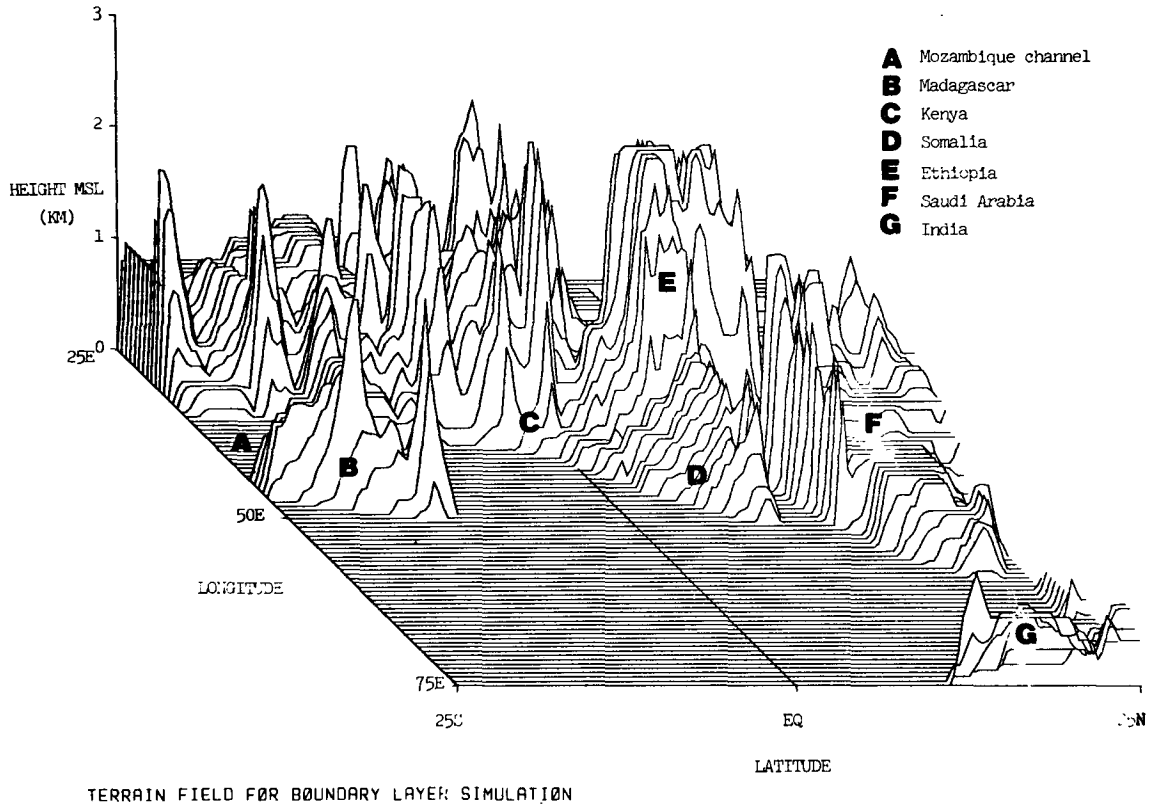

FIG. 6. Terrain field for boundary layer simulation.

vection terms are set to zero since the vertical velocity $w = 0$. The first level above the lower boundary where vertical advection terms are computed is level 2 (Fig. 5). This level is 165 m above level s and 200 m below level 3, and centered differences are used to evaluate the vertical advection.

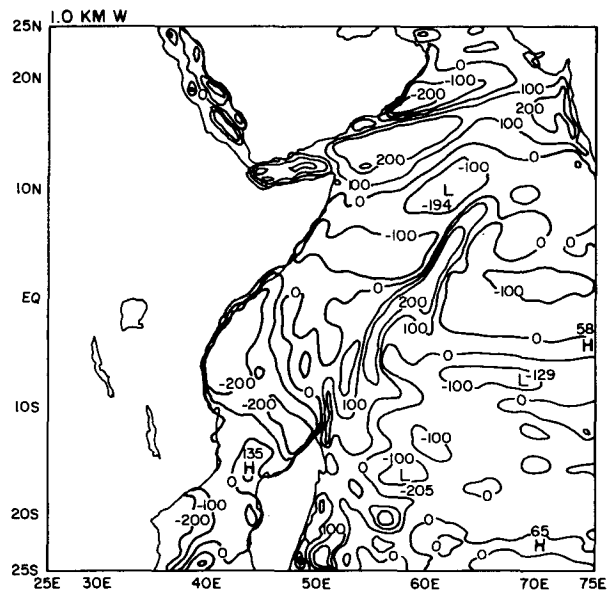

FIG. 7. Vertical velocity w ($\times 10^{-2}$ cm s^{-1}) at the 1 km level over the oceans. The land area is not shown because the full topography results in a rather cellular field.

The calculation of vertical velocity is carried out by a straightforward vertical integration of the mass continuity equation, utilizing the bottom boundary condition $w = 0$.

The initial state is constructed from the Ekman solution for a vertically averaged prescribed pressure gradient force and for an assigned value of $K = 10$ m^2 s^{-1}. This is done at all latitudes except within 5° of either side of the equator, where a linear interpolation of the Ekman solution at 5°S and 5°N is used.

The prescribed pressure gradients generate winds over the entire domain in the very first time step and by about day 18, the total kinetic energy for each layer varies by less than 0.01% between time steps. Further integration to 50 days produced no visible changes in the flow pattern. This behavior of the three-dimensional model is very similar to that of the two-dimensional model presented earlier.

3. The pressure field

Given the observed sea level pressure field and the temperature field at several vertical levels, the pressure field at the height levels of the model (Fig. 5) are

constructed using the hydrostatic law:

$$p_{K+1} = p_K \exp\left[-g/R \int_{Z_K}^{Z_{K+1}} T^{-1} dz\right], \quad (16)$$

where p_{K+1} is an upper level and p_K a lower level where the pressure is known. The observed temperature field T is obtained from a vertical interpolation of the analyzed fields at mandatory levels. The data sets include those from the World Weather Watch, dropwindsondes, research ships, sea level temperatures from commercial ships and soundings from TIROS N.

Figs. 8a, b, c illustrate the pressure field at sea level, 1.4 and 3 km levels for the MONEX data set for 27 June 1979. Similar pressure fields were available for the MONSOON 77 experiment. A strong surface pressure gradient is present over the Red Sea, across Somalia, and over the northern Arabian Sea. The heat low over Saudi Arabia appears as a trough on the surface charts. A ridge along the east African coast is an important region where cross-equatorial flow toward lower pressure occurs. The surface pressure gradient along the southern trades at 15°S is also well defined. The pressure gradients at the 1.4 and 3 km levels are much weaker in comparison to those at the surface (Figs. 8a, b, c). Because observed winds are strongest near the 1.4 km level, planetary boundary layer dynamics is important in this region. Over the northern Arabian Sea, the surface isobars have a slight tilt from southwest to northeast, except over the eastern Arabian Sea, while they are nearly zonal at 3 km. This veering of the geostrophic flow north of 10°N is consistent with Ekman dynamics.

Although similar structure of the pressure field was noted in the climatological and MONSOON 77 data

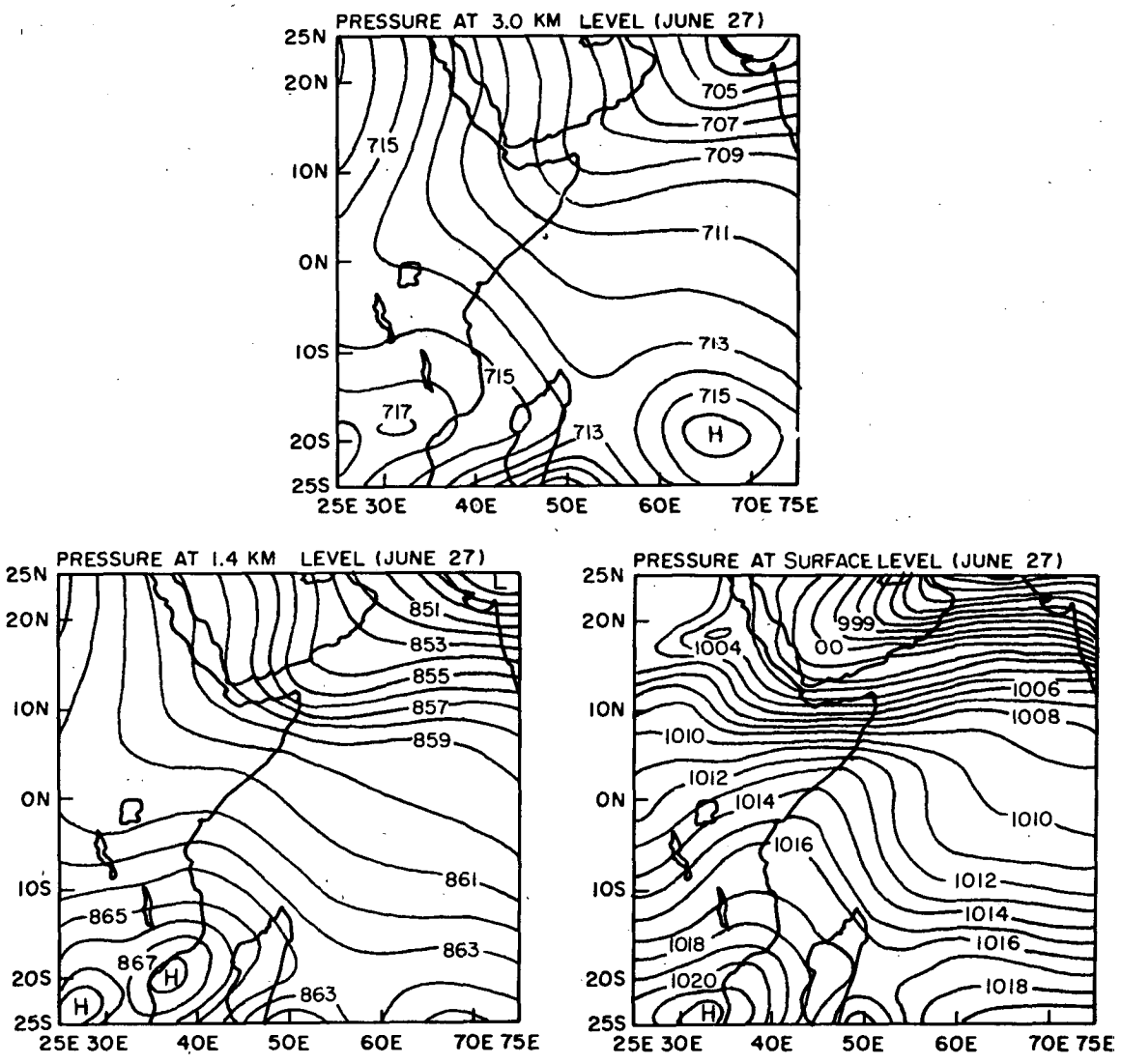

FIG. 8. Pressure field from the MONEX data set (1200 GMT 27 June 1979) at the surface, 1.4, and 3 km levels.

sets, the pressure field was much improved in MONEX due to the larger data set of surface pressure from merchant ships, soundings from drop-windsonde aircraft, TIROS N, and the World Weather Watch. The TIROS N data provide a horizontal resolution of the order of one sounding every 50 km, but do not provide a resolution better than 1.5 km in the verical. The composite analysis of the pressure field was based on careful hydrostatic checks, objective analysis using a successive correction method, with climatological values in the first guess, and a subjective correction of the final product. Fig. 9 illustrates the data locations for the composite observing systems during MONEX over the ocean.

4. Results of the model integrations

a. Horizontal displays of the motion field

The response of the wind field to the imposed pressure distribution appeared quite reasonable when compared to observations for the two experiments. An example of the details of the simulation for the MONSOON 77 experiment (1200 GMT 4 July 1977) is illustrated in Fig. 10. The streamlines (solid lines) and the isotachs (dashed lines, m s^{-1}) for the 1.4 km level show the principal features of the Arabian Sea circulation: strong meridional flow in the Mozambique channel, as noted by Hart *et al.* (1978) for that day; cross-equatorial flows; a strong low level Somali jet (intensity ~50 kt); and northwesterly flow over Arabia. The observed 850 mb wind data (kt) are plotted, where available, for comparison with the simulation. On the whole, this simulation of the horizontal distribution of the entire motion field is quite detailed and bears strong resemblance to the flows during an active monsoon (Krishnamurti *et al.*, 1979, 1980a, 1980b). Examples of the simulated (m s^{-1}) and observed (isotachs in m s^{-1}, data in kt) wind fields for the MONEX 1979 case (1200 GMT 27 June 1979) are presented in Figs. 11a and 11b, respectively. Here we compare the simulation at 1 km with the observed 850 wind analysis since (over the oceans) the latter is based largely on low cloud motions which fit best near the 1 km level. Many of the observed features of the flow are reproduced in the simulation, most notably the jet maximum southeast of Socotra. Next we shall discuss vertical cross-sections of the simulations.

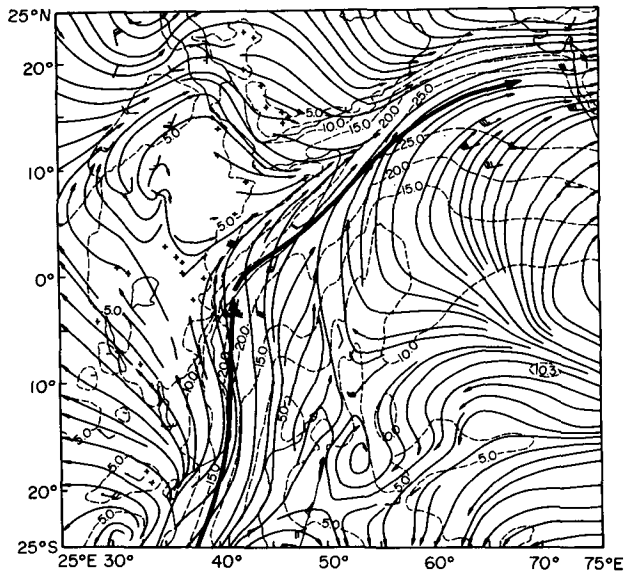

FIG. 10. Streamlines (solid lines) and isotachs (dashed lines, m s^{-1}) at 1.4 km for day 50 of the simulation for MONSOON 1977 (1200 GMT 4 July 1977). Observed 850 mb winds (kt) are plotted where available.

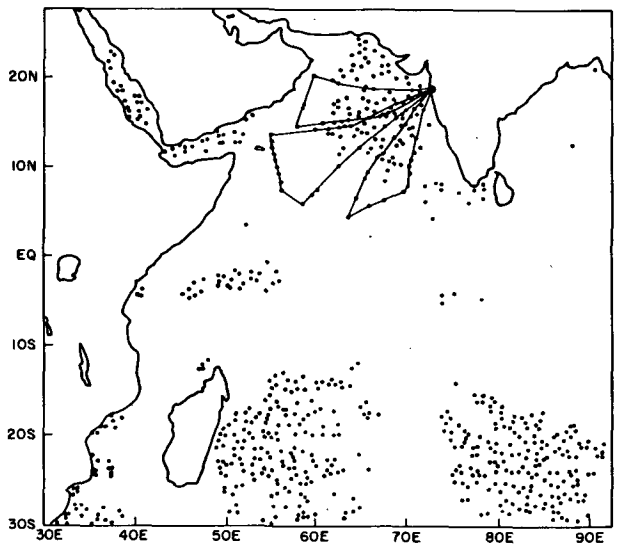

FIG. 9. Distribution of observation points over water for the composite MONEX observing system. Triangles indicate the tracks of three research aircraft.

b. Vertical cross-sections across the low level jet

Fig. 12 illustrates the zonal vertical cross sections of the meridional wind along 2°S for the MONSOON 77 Experiment. This case is illustrated because a detailed cross-section for the same period was available (Fig. 13) from observations (Hart *et al.*, 1978). The computed field is illustrated for the longitude belt 25 to 75°E, while the observed field extends only from 37 to 44°E. Overall, the boundary layer simulation of the cross-equatorial low level jet is in reasonable agreement with observations. A wind maximum of around 22 m s^{-1} is simulated at around the 1.5 km level which is slightly lower than the observed level (near 2 km) of the maximum wind. The observed as well as the calculated fields exhibit a strong vertical shear above the level of the maximum wind. The results shown here are sensitive to the choice of the upper boundary conditions, at z = 3 km. We believe that the slight discrepancy in the height of the max-

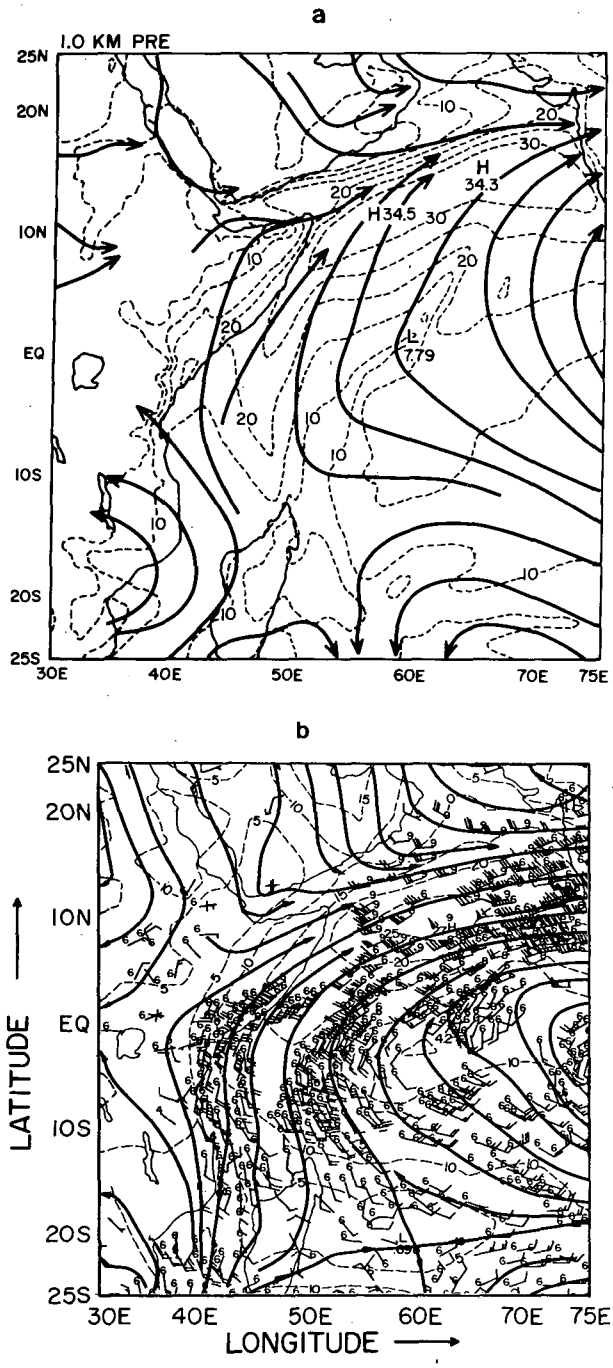

FIG. 11. (a) Streamlines (solid lines) and isotachs (dashed lines m s^{-1}) at 1 km for day 50 of the MONEX simulation (1200 GMT 27 June 1979); (b) Observed 850 mb winds (contours in m s^{-1}, wind barbs (kt) for the same time. Small numbers refer to data source (1–5 are radiosonde or pilot balloons, 6 and 7 are satellite winds, 8 is constant level balloon and 9 is research aircraft).

imum wind is related to a lack of proper coupling with the atmosphere above the 3 km level. This cross-section also illustrates the impact of the mountains; strong lateral shears of the meridional wind along the sloping terrain are reasonably simulated, although the observed lateral shear is slightly larger. The observed maximum wind occurs within a degree longitude from the coast. The model simulation exhibits the strongest comparable shear near 40°E (Fig. 12), probably reflecting the inadequacy of the ½° longitude mesh to fully resolve this feature.

During MONEX on 27 June 1979, the core of the Somali jet was extensively probed by the NOAA P-3 research aircraft. This enabled us to obtain detailed vertical cross-sections of the flow over the northwest Arabian Sea. Figs. 14a and b, respectively, depict the simulated and observed vertical cross-sections of isotachs of the total wind from 6.5 to 14°N (along 56.5°E) for the MONEX 1979 case. This includes the most intense portion of the jet. The agreement between the two cross-sections is generally good, although the simulated jet exhibits a speed maximum of ~67 kt, ~5 kt higher than that observed. Also, the simulated jet is located ~1° latitude farther north than the observed.

Similar results from the simulation of the low level jet were also obtained for the climatological data set, although detailed verifying observations are generally lacking.

c. *Turning of wind with height (The MONEX 1979 Experiment)*

Fig. 15 illustrates the turning of the wind with height between the 0.2 and 1 km level. The letter *B* denotes backing and *V* denotes veering. Of interest in this diagram are three regions of low level flows: the cross-equatorial flow, the low level jet, and the ITCZ.

No separation between backing and veering of wind with height is noted across the equator. The region, south of the low level jet over the entire domain, experiences a backing of wind with height. Stronger backing is found near the accelerating part of the low level jet over the western Arabian Sea. Across the equator, this meridional decrease of backing with height is consistent with stronger downward motions over the western Arabian Sea near 5°S. Maximum veering (or backing) angles are O(20°).

The jet is flanked by a region of backing of winds to its south, and very weak veering of wind with height to its north. This geometry is consistent with the low level momentum convergence along the jet in the planetary boundary layer. Along the jet, neither backing nor veering is noted.

The intertropical convergence zone, shown in Fig. 15a, is an asymptote of confluence that separates the air of continental origin and weak veering to its north from air of southern hemispheric origin, and weaker veering to its south. This geometry in the decelerating part of the flow is noted to experience low level convergence. A satellite photograph for 1200 GMT 27 June 1979 shown in Fig. 15b shows the cloud cover along this asymptote over the eastern Arabian Sea.

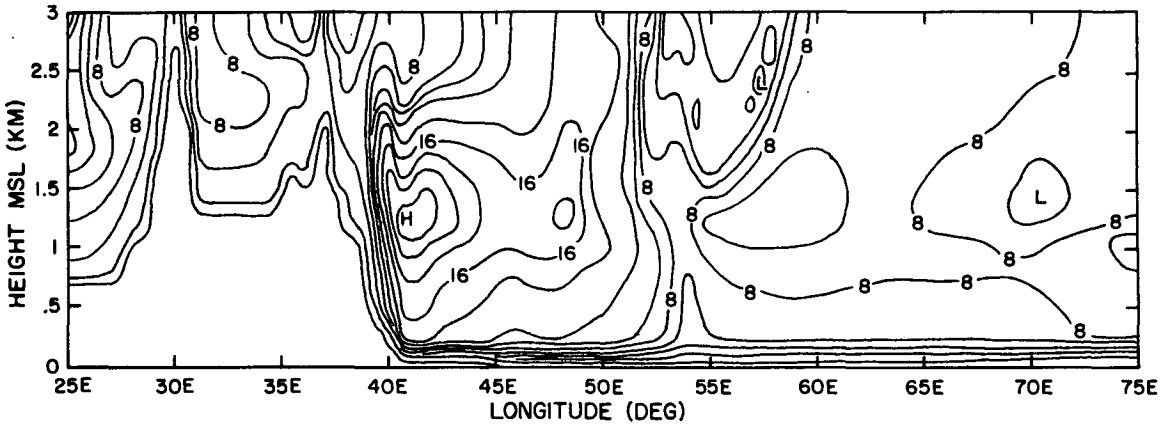

FIG. 12. Vertical-zonal cross-section of the meridional wind (m s^{-1}) along 2°S for the MONSOON 1977 simulation at day 18.

d. The balance of forces

The balance of forces for the MONEX experiment at the 0.2 and 1 km levels is illustrated in Figs. 16a and b. Our notation for the balance is expressed by

$$w\frac{\partial \mathbf{V}}{\partial z} + (\mathbf{V}_H \cdot \nabla)\mathbf{V}_H + f\mathbf{V}_H \times \mathbf{k} + \frac{1}{\rho}\nabla p + \mathbf{F} = 0.$$

(1) (2) (3) (4) (5)

We include only vectors of terms whose "relative force" (*i.e.*, the ratio of the vector magnitude of a given term to the vector magnitude of the largest term in the balance) exceeds a magnitude of 0.3. Because it is not possible to illustrate the vectors for all of the 10 201 grid points on a horizontal plane, it was decided to show the vectors at a 5° latitude/longitude resolution. At the lower (0.2 km) level (Fig. 16a), the Ekman balance (terms 3 + 4 + 5 ≈ 0) is clearly evident north of 10°N, and south of 10°S. The following comments on the notation are pertinent here. In this notation, the vector sum at a point vanishes. For a balance among pressure gradient, friction and advective acceleration, and if the sum of the pressure gradient (4) and friction (5) is an eastward directed force, then the horizontal acceleration (2) is displayed as a westward directed vector to illustrate the balance. We shall next examine the three regions of interest over the Arabian Sea.

The confluence line of the intertropical convergence zone is zonally oriented along ~12.5°N (Fig. 16b). The balance of forces across this line shows a comparatively stronger role of the Coriolis force (3) on its poleward side at the 0.2 km level. Here, the stronger Coriolis force is identified by a balance among *C*, *P* and *F* (*i.e.*, 3, 4 and 5) in Fig. 16a along 15°N. Along 10°N, the Coriolis force is somewhat weaker and the frictional (relative) force is somewhat stronger. The stronger veering of wind at 15°N is partly attributed to the stronger Coriolis force and the

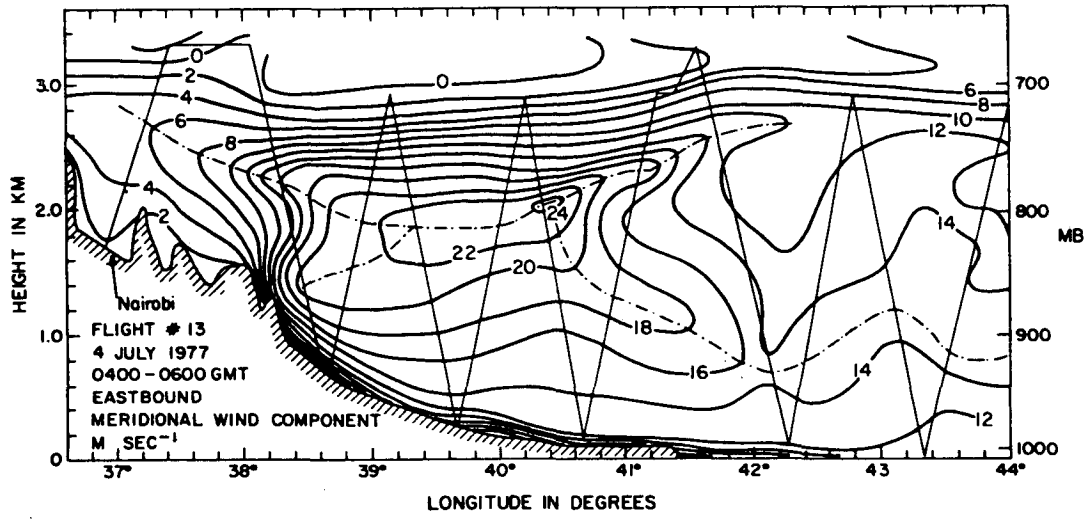

FIG. 13. As in Fig. 12, but for observed meridional wind from 37–44°E.

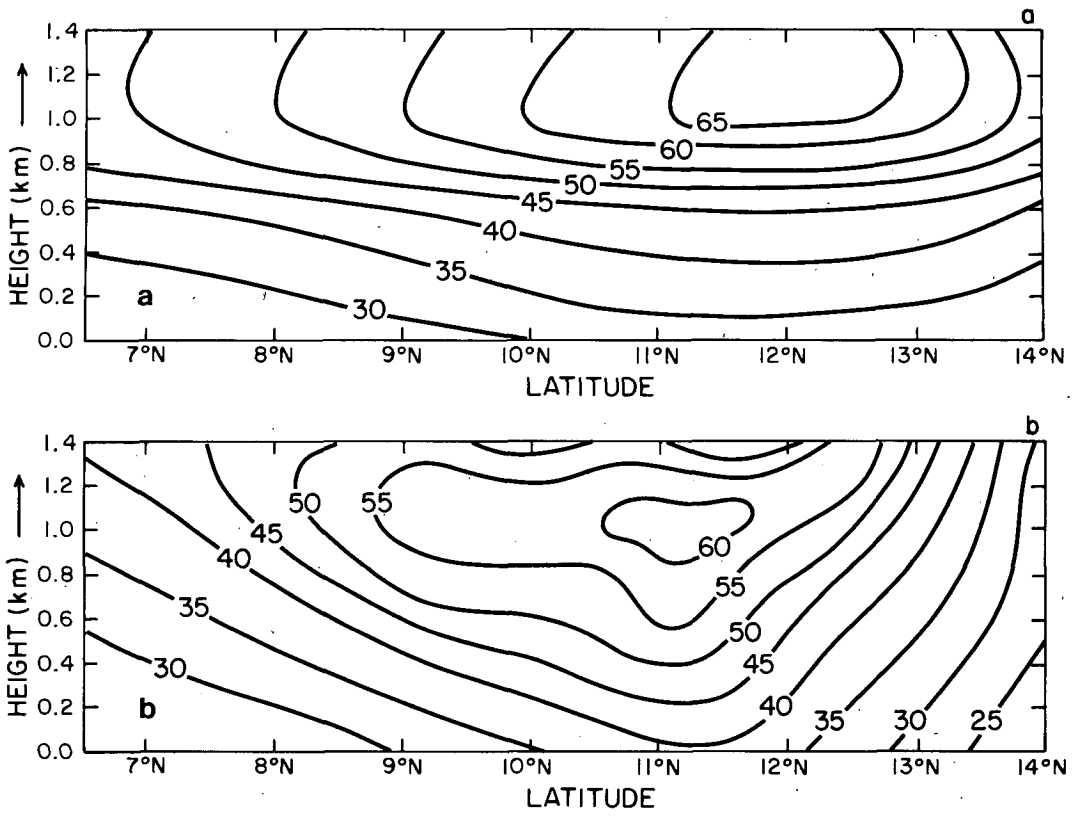

FIG. 14. Simulated (a), and observed (b), vertical-meridional cross-section of total wind speed (kt) for the MONEX (1979) case along 56.5°E.

weaker veering at 10°N may be attributed to both the weaker Coriolis force and to the somewhat stronger frictional force. The latter balance favors a non-geostrophic flow towards lower pressure to the north. Thus the low level confluent geometry of the ITCZ is maintained by an Ekman balance on its poleward side and an advective balance with a stronger cross-isobaric flow on its equatorward side.

At the 1 km level (Fig. 16b), the frictional (relative) force (5) is small over the oceanic region. North of the asymptote of convergence, a geostrophic balance ($3 + 4 \approx 0$) is found over the northern Arabian Sea. To its south, along 10°N, the advective acceleration (2) becomes important. The acceleration vector turns more and more from the north between the equator (at 45°E) and 15°N (at 65°E) as one proceeds downstream. This clockwise turning of the acceleration vector contributes to the confluence along 10 to 15°N. The geostrophic flow (which is perpendicular to the pressure force (4) shown in Fig. 16b) cannot account for the confluence. Thus we note (as we also noted in Krishnamurti and Wong, 1979) that the ITCZ is located in a region with geostrophic balance ($3 + 4 \approx 0$) to its north and an advective balance to its south at the 1 km level.

If we consider a point in the accelerating part of the jet (*e.g.*, 10°N, 55°E), the relative lack of veering or backing of wind with height may be attributed to a relative increase of the advective acceleration and a decrease of the frictional force between the 0.2 and 1 km level. To the south of the jet axis (*e.g.*, 5°N, 55°E), the frictional force is directed towards the southwest at the 0.2 km level while at 1 km the advective acceleration is directed in a due southerly direction. The flows at the respective levels are nearly opposite to these, so that a backing of wind with height results. To the immediate south of the convergence zone (10°N, 55°E), the frictional force is directed along a south-southwesterly direction, while at the 1 km level the flow exhibits an essential balance between the Coriolis, pressure gradient and advective accelerations; the latter is directed towards the southwest.

Near the equator the Somali jet identified in Fig. 15 is found just south of the asymptote of convergence. Young (1981) distinguishes the accelerating part from the decelerating part of the low level jet. In Fig. 16b we note an analogous orientation of the vector in the accelerating part of the jet. The decelerating part is not as conspicuous since the jet on 27 June extended almost to 70°E. The location of the jet axis along 12.5°N over the Arabian Sea is largely determined by the prescribed pressure gradient field (vector 4) in that region. An additional factor that can be seen in the vector balance diagram is the stronger equatorward frictional (relative) force

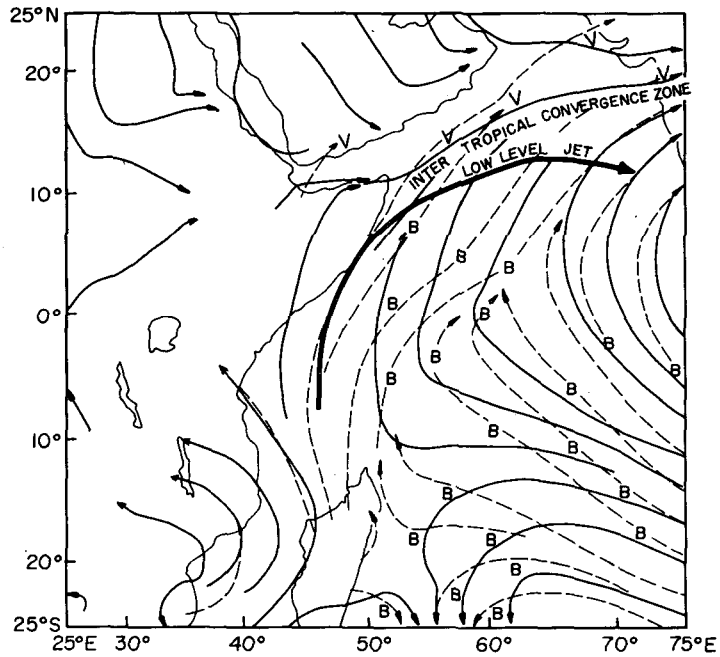

FIG. 15 a. Regions of veering (*V*) and backing (*B*) of the wind between 0.2 and 1 km for the MONEX (1979) simulation. Solid and dashed lines are 1 and 0.2 km streamlines, respectively. Heavy line is axis of 1 km isotach maximum. Open areas are regions of terrain exceeding 1 km.

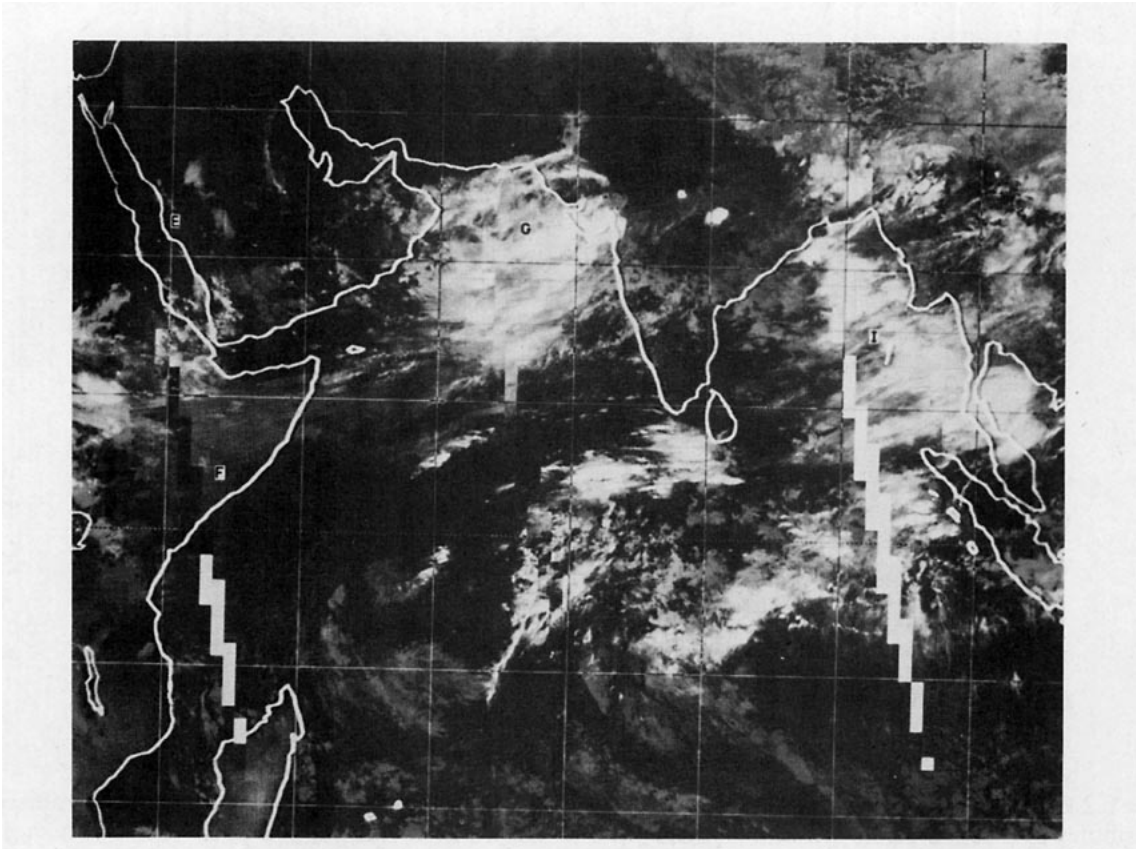

FIG. 15b. A satellite infrared photograph illustrating the intertropical convergence zone over the northern Arabian Sea for 27 June 1979. This picture corresponds to the period of the flow field shown in Fig. 11b.

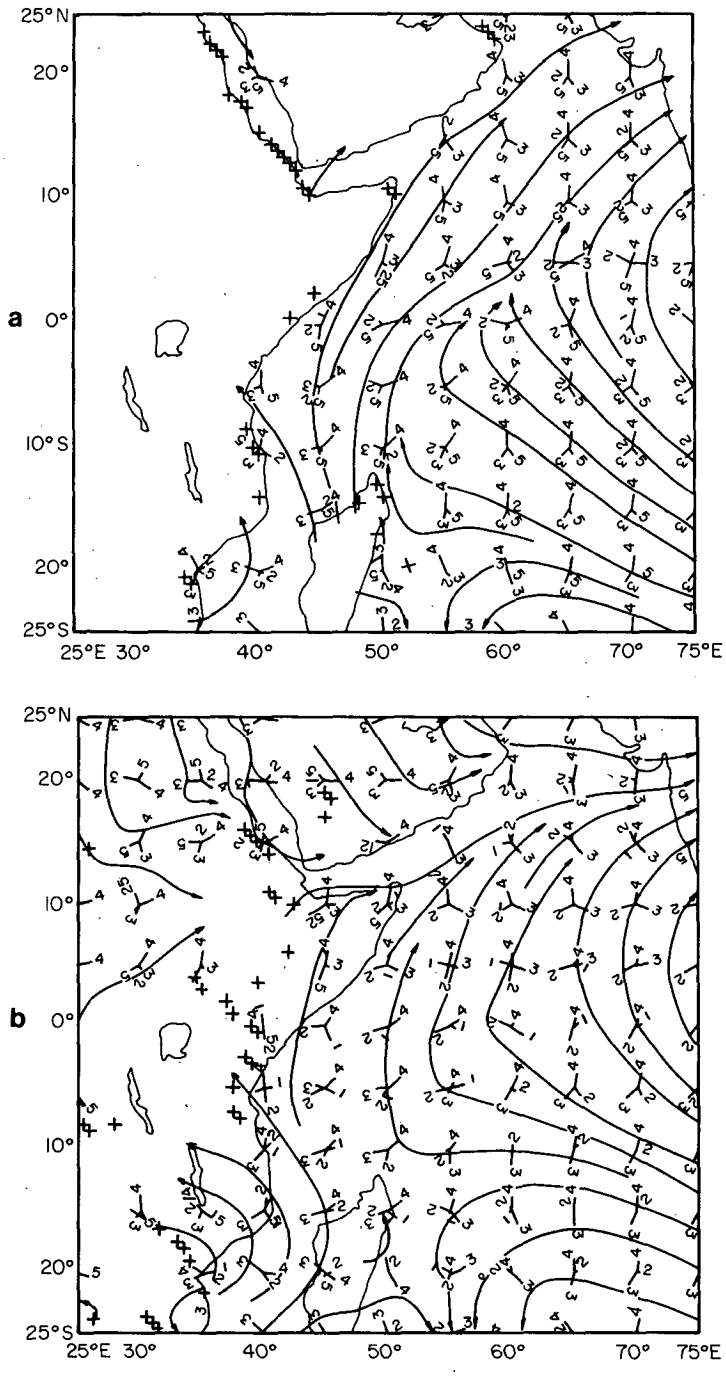

FIG. 16. Balance of forces at (a) 0.2 km, and (b) 1 km for the MONEX simulation. The numbers 1 through 5 represent, respectively, vertical advection, horizontal advection, Coriolis, pressure gradient, and frictional forces. The length of each line is proportional to the "relative force" (Mahrt, 1972). Only relative forces exceeding 0.3 are shown at a given point. Cross marks denote zero wind speed.

at the 0.2 km level at 15°N compared to 10°N, which contributes to a convergence of flux of westerly momentum around 12.5°N.

In the equatorial region near the east African coast, vertical advection, due to strong downward motions, has an important role over the western Arabian Sea. The vertical wind shear is positive in this region (*i.e.*, southerly winds increase with height) and the downward motions contribute to a net acceleration of the southerly wind. The vertical acceleration vector, in

our notation, is thus directed southward (Fig. 16b). This region of stronger downward motions at 1 km is indicated by the isopleths in Fig. 7. Vertical advection diminishes eastward over the Arabian Sea. In this region, the advective boundary layer shows an essential balance between pressure gradient (4), horizontal advection (2), and vertical advection (1). The region between the equator at 5°N over the western Arabian Sea is of considerable interest because of the acceleration of the winds as we approach the Somali jet. In this example, the strong winds extend to ~65°E, much farther east than the climatological position. In the context of the present numerical experiment, this can be viewed as a response of the flows to the prescribed strong pressure gradient. Lacking a substantial Coriolis effect, the response is a strong meridionally directed flow with an essential balance among friction, advection and pressure gradient forces at the lowest levels, and advection and the pressure gradient forces at the 1 km level.

5. Concluding remarks

If future observing systems provide detailed surface pressure data from an enhanced World Weather Watch and marine ships of opportunity, then they could be combined with high resolution temperature data sets derived *via* satellite to provide a detailed definition of the three-dimensional mass distribution. A high resolution fine-mesh boundary layer model, such as the one described here, can utilize this information to provide an equilibrium motion field of considerable detail. This model output could be further used to provide boundary layer input of the motion field for larger prediction models. The value of the model in its present form is restricted to those cases where mass field data is abundant and wind field data more limited. Eventually, it would be desirable to incorporate wind data as well, in the form of a four-dimensional data assimilation for the planetary boundary layer. This work is currently in progress.

The use of K-theory for a near-neutral PBL (Krishnamurti and Wong, 1979) is, of course, a limitation of this work; furthermore, the validity of this model to situations where the temporal changes are large is questionable. The experiments for this study were selected carefully to avoid such situations. Future extensions of the model will address these shortcomings.

The present study has successfully simulated an equilibrium motion field using a horizontal resolution of 55 km and a vertical resolution of 200 m. The structure of the cross-equatorial low level Somali jet agrees reasonably with aircraft observations made during the two monsoon experiments. This study has revealed interesting transitions in the intensity of the backing and veering of wind with height across the Somali jet and the intertropical convergence zone. In the former region, momentum convergence results from the backing of winds to the south of the jet axis and weak veering of winds to its north. The mass convergence in the intertropical convergence zone is found along a line of confluence where weak veering occurs to its north and weaker veering is found to its south. This geometry is consistent with a deep layer of confluence in the planetary boundary layer. The equatorial regions over the western Arabian Sea encounter strong descending motions. Here a strong backing of winds to the south, and a weaker backing of winds to the north (i.e., a meridional gradient of backing of wind) is noted. The detailed balance of forces examined at 0.2 and 1 km reveal a substantial decrease of the frictional relative force with height. The turning of wind described in different regions appears consistent with the computed balances, as it should be.

The region north of the ITCZ (Fig. 15a) shows an essential Ekman balance with a veering of wind with height. The region between the ITCZ and the low level jet shows a weak role for the horizontal advective acceleration that contributes to a relative decrease of the veering of wind with height. Along the jet axis, the decrease of frictional relative force with height and a proportionate relative increase of advective acceleration results in neither veering nor backing of winds. The western equatorial region experiences a downward flux of southerly momentum that results in a weaker backing of wind compared to the region farther south where a stronger backing is noted. The geometry is consistent with the diffluence and downward motion in the region immediately south of the equator.

Computationally, this was a large exercise in modeling. It required integration of a rather high resolution model (10 201 × 16 grid points). This was accomplished to provide the steady state solution in the presence of steep mountains utilizing the no-slip conditions. The precise role of the individual mountains (Fig. 6) requires many further experiments.

Acknowledgments. The authors wish to convey their appreciation to Professor John Young for many helpful comments. Appreciation is also expressed to Professor N. E. LaSeur for providing Fig. 14b which is based on detailed MONEX data analysis.

This work was jointly supported by the National Science Foundation and the National Oceanic and Atmospheric Administration under Grant ATM-7819363. Computations for this work were carried out on the Florida State University CYBER and the National Center for Atmospheric Research CRAY systems. National Center for Atmospheric Research is sponsored by the National Science Foundation.

APPENDIX

List of Symbols and Acroynyms

A magnitude of advection of momentum
B magnitude of Coriolis acceleration
C_D drag coefficient

F magnitude of frictional dissipation of momentum
F_x frictional dissipation of u
F_y frictional dissipation of v
$\mathbf{F}$ vectorial frictional dissipation
f Coriolis parameter
g acceleration of gravity
H magnitude of horizontal advection of momentum
h terrain height
K vertical eddy diffusion coefficient
k von Karman constant, also friction coefficient
p pressure
P magnitude of pressure gradient acceleration
R gas constant of dry air
T temperature, also magnitude of local time rate of change of momentum
t time
t' non-dimensional t
U scale factor for u and v
u zonal velocity
u' non-dimensional u, also deviation of u from time mean u
V magnitude of vertical acceleration of momentum
$\mathbf{V}_b$ vector motion along balloon trajectory
$\mathbf{V}_G$ surface wind vector from ECMWF analysis
$\mathbf{V}_H$ horizontal velocity
$\mathbf{V}_s$ horizontal velocity at top of surface layer
$|\mathbf{V}_s|$ magnitude of V_s
$\mathbf{V}_+$ horizontal velocity at top of the layer above the surface layer
v meridional velocity
v' non-dimensional v, also deviation of v from time mean v
w vertical velocity
w' non-dimensional w, also deviation of w from time mean w
x east–west coordinate
x' non-dimensional x
y north–south coordinate
y' non-dimensional y
Z_s geopotential height at top of surface layer
Z_+ geopotential height at top of the layer above the surface layer
z vertical coordinate
z_0 surface roughness length
z' non-dimensional z
$\bar{}$ overbar denotes time average
β northward variation of Coriolis parameter f
ϵ energy dissipation
ϕ geopotential on a constant pressure surface
λ dissipation length scale
ρ density
ζ magnitude of eddy momentum flux
ω scale factor for t

BALSAMINE BALlons Surpressurisés pour l'Analyse de la Mousson INdienne d'Eté
ECMWF European Centre for Medium Range Weather Forecasts
FGGE First Global Experiment of the Global Atmospheric Research Programme
MONEX MONsoon EXperiment
NOAA National Oceanic and Atmospheric Administration

REFERENCES

Fiedler, F., and H. Panofsky, 1972: The geostrophic drag coefficient and the effective roughness length. *Quart. J. Roy. Meteor. Soc.*, **98,** 213–220.

Gates, W. L., and A. B. Nelson, 1975: A new (revised) Tabulation of the Scripps topography on a 1° global grid. Part I: Terrain heights. Report No. R-1276-1-ARPA: Rand Corporation, 1–132.

Hart, J. E., G. V. Rao, H. Van de Boogaard, J. A. Young and J. Findlater, 1978: Aerial observations of the east African low-level jet stream. *Mon. Wea. Rev.*, **106,** 1714–1724.

Krishnamurti, T. N., and V. Wong, 1979: A simulation of cross-equatorial flow over the Arabian Sea. *J. Atmos. Sci.*, **36,** 1895–1907.

——, P. Ardanuy, Y. Ramanthan and R. Pasch, 1979: Quick look summer MONEX atlas, Part II: The onset phase. Report No. 79-5, Dept. of Meteorology, Florida State University, 205 pp.

——, P. Greiman, Y. Ramanthan, R. Pasch and P. Ardanuy, 1980a: Quick look summer MONEX atlas, Part I: Saudi Arabia phase. Report No. 80-4, Dept. of Meteorology, Florida State University, 71 pp.

——, Y. Ramanathan, P. Ardanuy, R. Pasch and P. Greiman, 1980b: Quick look summer MONEX atlas. Part III: Monsoon Depression phase. Report No. 80-8, Dept. of Meteorology, Florida State University, 135 pp.

Mahrt, L. J., 1972: A numerical study of the influence of advective accelerations in an idealized, low latitude, planetary boundary layer. *J. Atmos. Sci.*, **36,** 1477–1484.

——, and J. A. Young, 1972: Some basic theoretical concepts of boundary layer flow at low latitudes. *Dynamics of the Tropical Atmosphere,* NCAR, 411–420.

Miyake, M., M. Donelan, G. McBean, C. Paulson, F. I. Badgley and E. Leavitt, 1970: Comparison of turbulent fluxes over water determined by profile and eddy correlation techniques. *Quart. J. Roy. Meteor. Soc.*, **96,** 132–137.

Reverdin, G., and G. Sommeria, 1981: Dynamics of the tropical boundary layer as deduced from constant level balloon trajectories over the Indian Ocean. *Proc. Int. Conf. on Early Results of FGGE and Large Scale Aspects of its Monsoon Experiments.* Tallahassee, WMO, 12.12–12.16.

Rubinstein, D. M., 1981: The daytime evolution of the East African Jet. *J. Atmos. Sci.*, **38,** 114–128.

van de Boogaard, H., 1977: The mean circulation of the tropical and subtropical atmosphere, July. Tech. Report, NCAR-TN-118+STR, 48 pp. [Available from the National Center for Atmospheric Research, Boulder, CO].

Wyngaard, J. C., and K. S. Rao, 1974: Modeling the atmosphere boundary layer. *Advances in Geophysics,* **18A,** Academic Press, 193–211.

Young, J., 1981: Low level summer monsoon circulations. *Proc. Int. Conf. on Early Results of FGGE and Large Scale Aspects of its Monsoon Experiments.* Tallahassee, WMO, 4.5–5.11.